

Experimental observation of topological Fermi arcs in type-II Weyl semimetal MoTe_2

Ke Deng^{1†}, Guoliang Wan^{1†}, Peng Deng^{1†}, Kenan Zhang¹, Shijie Ding¹, Eryin Wang¹, Mingzhe Yan¹, Huaqing Huang¹, Hongyun Zhang¹, Zhilin Xu¹, Jonathan Denlinger², Alexei Fedorov², Haitao Yang^{1,3}, Wenhui Duan^{1,4}, Hong Yao^{4,5}, Yang Wu^{3*}, Shoushan Fan^{1,3,4}, Haijun Zhang^{6,7}, Xi Chen^{1,4*} and Shuyun Zhou^{1,4*}

Weyl semimetal is a new quantum state of matter^{1–12} hosting the condensed matter physics counterpart of the relativistic Weyl fermions¹³ originally introduced in high-energy physics. The Weyl semimetal phase realized in the TaAs class of materials features multiple Fermi arcs arising from topological surface states^{10,11,14–16} and exhibits novel quantum phenomena, such as a chiral anomaly-induced negative magnetoresistance^{17–19} and possibly emergent supersymmetry²⁰. Recently it was proposed theoretically that a new type (type-II) of Weyl fermion^{21,22} that arises due to the breaking of Lorentz invariance, which does not have a counterpart in high-energy physics, can emerge as topologically protected touching between electron and hole pockets. Here, we report direct experimental evidence of topological Fermi arcs in the predicted type-II Weyl semimetal MoTe_2 (refs 23–25). The topological surface states are confirmed by directly observing the surface states using bulk- and surface-sensitive angle-resolved photoemission spectroscopy, and the quasi-particle interference pattern between the putative topological Fermi arcs in scanning tunnelling microscopy. By establishing MoTe_2 as an experimental realization of a type-II Weyl semimetal, our work opens up opportunities for probing the physical properties of this exciting new state.

In the Brillouin zone of a type-I Weyl semimetal, the linearly dispersing and non-degenerate bands cross each other at the Weyl points (Fig. 1a). These band-topology protected Weyl points can be created or annihilated only in pairs according to the no-go theorem¹. When projected onto the surface, the Weyl points are connected by the topologically protected Fermi arcs (Fig. 1a)². In contrast to the type-I Weyl fermions in the TaAs class or compressively strained HgTe ¹² that have a point-like Fermi surface, the type-II Weyl fermions emerge at the boundary between electron and hole pockets when the cones are tilted significantly (Fig. 1b), and there is a finite density of states at the Fermi energy E_F . The distinction between the Fermi surfaces of these two types of Weyl semimetal is expected to lead to different physical properties and response to magnetic fields²¹.

Type-II Weyl fermion has been predicted in the orthorhombic T_d phase of WTe_2 (ref. 21), which breaks the inversion symmetry and shows unusual transport properties²⁶. However, the small

momentum separation of the Weyl points (0.7% of the Brillouin zone) and the extremely small size of the arcs²¹ make it exceptionally challenging to resolve the topological Fermi arcs in WTe_2 by angle-resolved photoemission spectroscopy (ARPES). A promising solution is provided by the prediction that the topological Fermi arcs can be significantly enlarged in MoTe_2 (refs 23,24) or $\text{Mo}_x\text{W}_{1-x}\text{Te}_2$ (ref. 27). Among these candidate materials, MoTe_2 is particularly interesting because of the reported superconductivity²⁸ and the predicted topological phase transition induced by temperature or strain²³. Although the electronic structures of WTe_2 (refs 29–31) and $\text{Mo}_x\text{W}_{1-x}\text{Te}_2$ (ref. 32) have been experimentally studied, so far there is no conclusive evidence on the existence of topological Fermi arcs. Here, by combining two complementary surface-sensitive probes—ARPES and scanning tunnelling microscopy (STM), we provide direct experimental evidence of the topological Fermi arcs at the boundary between electron and hole pockets in the T_d phase of MoTe_2 , establishing it as a type-II Weyl semimetal.

MoTe_2 is polymorphic with three different structures: hexagonal (α -phase, or 2H phase), monoclinic (β -phase, or $1T'$ phase) and orthorhombic (γ -phase, or T_d phase). The $1T'$ phase has a distorted CdI_2 structure (Fig. 1c) that crystallizes in the centrosymmetric space group $P2_1/m$. The Mo atoms are coordinated by six Te atoms but shifted from the centre of the Te octahedra, resulting in the zigzag chains along the b axis. The bonding between the shifted Mo atoms corrugates the Te sheets and distorts the Te octahedra^{33,34}, causing the c axis to incline at an angle of $\sim 93.9^\circ$ (ref. 33). A temperature-induced phase transition from the high-temperature $1T'$ to the low-temperature T_d phase has been reported between 240 K to 260 K (ref. 33). The T_d phase (Fig. 1d) shares the same in-plane crystal structure (Fig. 1e) as the $1T'$ phase but has a vertical (90°) stacking and belongs to the non-centrosymmetric space group $Pmn2_1$. Weyl fermions are possible in the T_d phase only where the inversion symmetry is broken. The Brillouin zone of the T_d phase is shown in Fig. 1f.

Figure 1g shows the X-ray diffraction intensity of the high-quality MoTe_2 single crystal at room temperature ($1T'$ phase). The Raman spectrum in Fig. 1h shows A_g vibrational modes at ~ 160 and 260 cm^{-1} (ref. 35). The resistance measurement (Fig. 1i) confirms the first-order phase transition between the T_d and $1T'$ phases at $\sim 260\text{ K}$, in agreement with previous results³³. The high

¹State Key Laboratory of Low Dimensional Quantum Physics and Department of Physics, Tsinghua University, Beijing 100084, China. ²Advanced Light Source, Lawrence Berkeley National Laboratory, Berkeley, California 94720, USA. ³Tsinghua-Foxconn Nanotechnology Research Center, Tsinghua University, Beijing 100084, China. ⁴Collaborative Innovation Center of Quantum Matter, Beijing, China. ⁵Institute for Advanced Study, Tsinghua University, Beijing 100084, China. ⁶National Laboratory of Solid State Microstructures and School of Physics, Nanjing University, Nanjing 210093, China. ⁷Collaborative Innovation Center of Advanced Microstructures, Nanjing, China. [†]These authors contributed equally to this work.

*e-mail: wuyangthu@mail.tsinghua.edu.cn; xc@mail.tsinghua.edu.cn; syzhou@mail.tsinghua.edu.cn

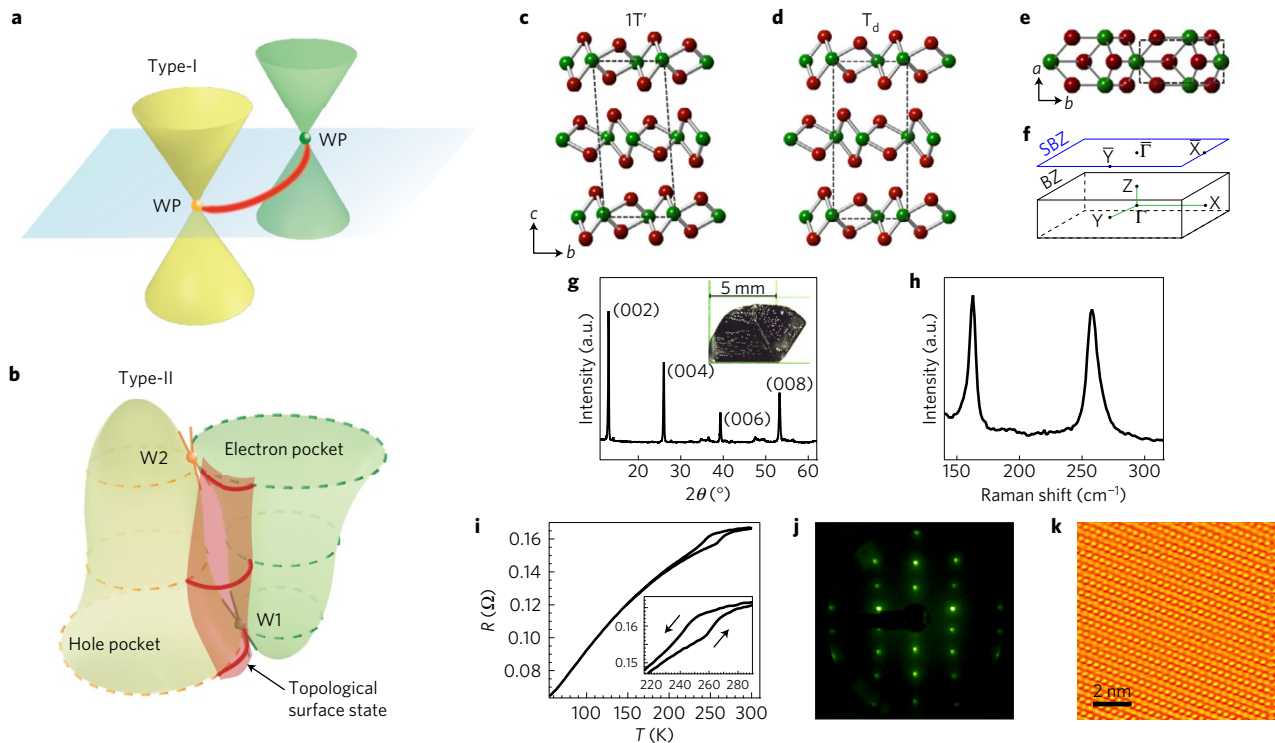


Figure 1 | Characterization of type-II Weyl semimetal MoTe₂. **a**, Dispersions for type-I Weyl fermion near E_F . The Weyl points (WP) are labelled by yellow and green dots. **b**, Type-II Weyl semimetal with electron and hole pockets touching at two different energies. **c, d**, Crystal structures of MoTe₂ in the 1T' (**c**) and T_d (**d**) phases. Green balls are Mo atoms and red balls are Te atoms. **e**, The in-plane crystal structure. **f**, Bulk and projected surface Brillouin zone. **g**, X-ray diffraction of MoTe₂ measured at room temperature (1T' phase). The inset shows a picture of the few-millimetre-size single crystal. **h**, Raman spectrum measured at room temperature. **i**, Transport measurement shows a first-order phase transition between the 1T' phase and the T_d phase. **j**, Low-energy electron diffraction pattern taken in the T_d phase at beam energy of 180 eV. **k**, The STM topography (bias -50 mV, tunnelling current 0.05 nA) taken at 4.2 K.

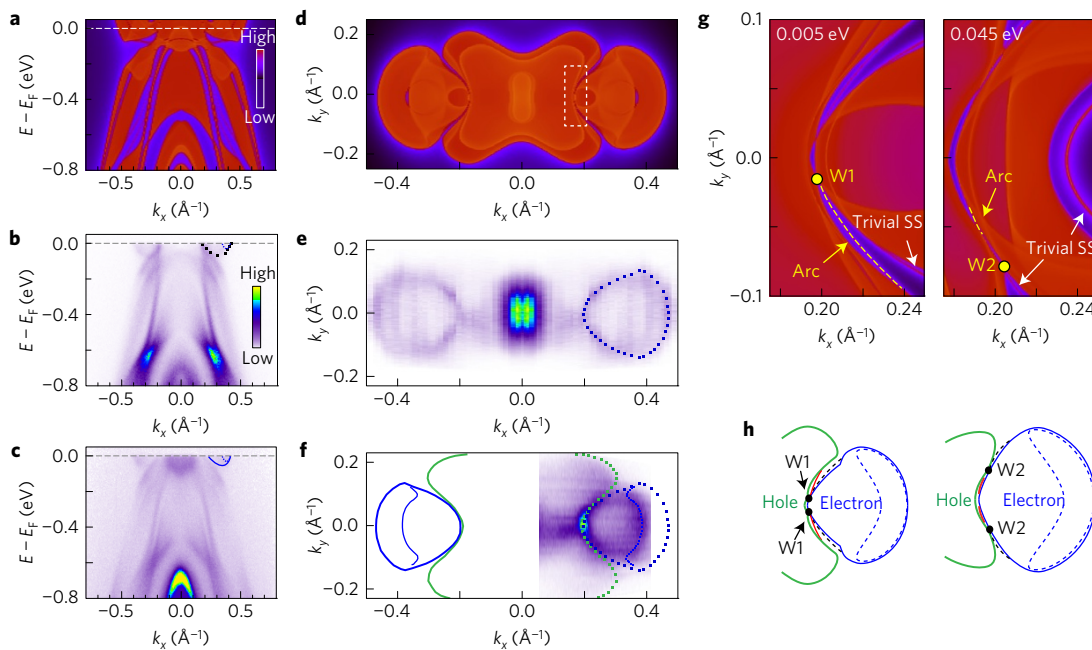


Figure 2 | Band structure of MoTe₂. **a**, Calculated dispersion along the $\bar{X}-\bar{\Gamma}-\bar{X}$ direction. **b, c**, Measured dispersions along the $\bar{X}-\bar{\Gamma}-\bar{X}$ direction with horizontal (p) and vertical (s) polarizations at photon energy of 32.5 eV. A comparison of calculated band structure with experimental dispersions shows that the sample is slightly hole doped, and the calculated energy needs to be shifted by -0.02 eV. **d**, Calculated spectral function at E_F . **e, f**, Intensity maps measured at E_F with p polarization using a 6.3 eV laser source with light polarizations perpendicular to the b and a axis respectively. The map in **e** was obtained by symmetrizing the data taken at positive k_x values. The electron and hole pockets are highlighted by blue and green colour. **g**, Calculated spectral function at 0.005 eV and 0.045 eV. The range of momentum is marked by the dashed rectangle in **d**. The Weyl points and topological Fermi arcs are highlighted. **h**, Schematic showing the different electronic structures at the Weyl points W1 and W2.

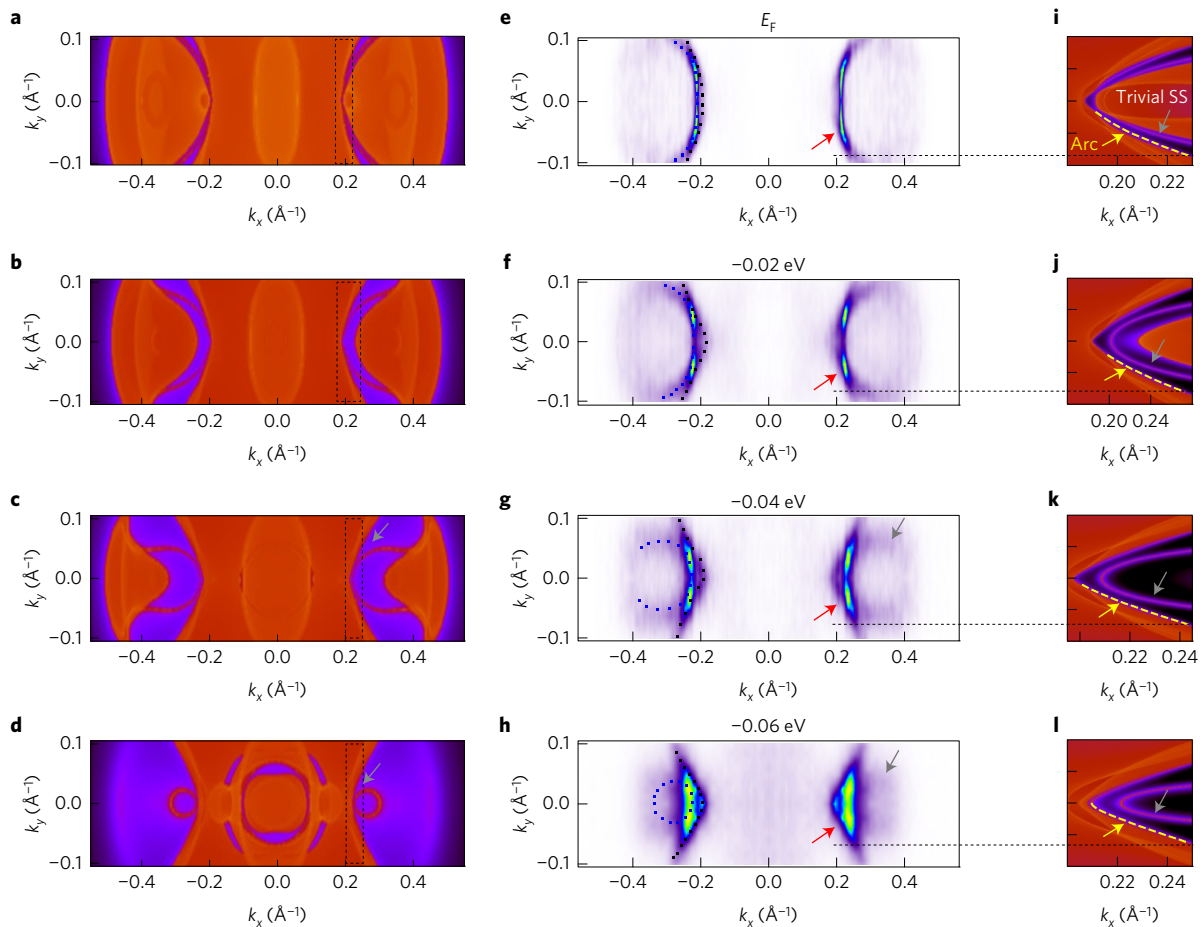


Figure 3 | Observation of topological Fermi arcs in the T_d phase of MoTe_2 . **a–d**, Calculated spectral intensity maps (shifted by -0.02 eV to account for the slight hole doping). The rectangles mark the regions that are enlarged in **i–l**. **e–h**, ARPES intensity maps at energies from E_F to -0.06 eV. The maps were symmetrized with respect to k_y and k_x . Red and grey arrows point to the topological and trivial surface states, respectively. **i–l**, Zoom-in of the rectangular regions in **a–d** to show the arcs from the topological surface states. The arcs at negative k_y are highlighted by yellow broken curves. Yellow arrows point to topological surface states and grey arrows point to trivial surface states. Black dotted lines are guides to the eye for the termination points of the arcs from ARPES measurement and calculation.

crystallinity of the samples is revealed by the sharp diffraction spots (Fig. 1j) in the low-energy electron diffraction pattern measured on a freshly cleaved sample in the T_d phase. The atomically resolved STM topography in Fig. 1k further confirms the high quality of the MoTe_2 crystal. The cleaved surface is terminated by Te atoms. The image shows a rectangular lattice with the lattice constants of $a = 3.5$ Å, $b = 6.3$ Å. The centre and corner atoms of a rectangular unit are different in height and exhibit distinct contrast. The dI/dV spectrum on the surface is shown in the Supplementary Information.

Figure 2a–c compares the electronic structure of MoTe_2 in the T_d phase measured by ARPES with band structure calculation along the a -axis ($\bar{X}-\bar{\Gamma}-\bar{X}$) direction. In band structure calculation, the bands with significant k_z dispersion overlap to form continuously filled contours, while those with strong surface state characteristics show up as sharp features in the intensity maps. The ARPES spectral intensity is affected by the dipole matrix elements and thereby depends on both the electron wavefunction and light polarization. To resolve the dispersions of multiple pockets, we use UV light with both horizontal (p) and vertical (s) polarizations. The measured dispersions (Fig. 2b,c) are in good agreement with the first-principles calculations (Fig. 2a). The trivial surface states (marked by the black broken curve) together with the smaller electron pocket (blue broken curve) are better resolved with the p -polarization light (Fig. 2b), while the s -polarization light (Fig. 2c) clearly resolves

both bulk electron pockets (blue solid and dotted curves) and the pocket surrounding the Γ point. In the calculated spectral function (Fig. 2d), the spectral weight of the electron pockets forms bell-like shapes on both sides away from the Γ point and part of the bowtie-shaped outer contour around the Γ point is contributed by the hole pockets at E_F . These bulk states are better observed with a bulk-sensitive laser source at 6.3 eV (penetration depth of ≈ 30 Å) in ARPES. Figure 2e,f shows the measured Fermi surface maps with light polarizations perpendicular to the b and a axis respectively. The bulk electron pockets are clearly observed in Fig. 2e and have an overall uniform intensity contour (blue broken curve), while the bowtie-shaped hole pocket is more clearly observed in Fig. 2f (green curve).

According to band structure calculation (Fig. 2g), the above observed electron and hole pockets touch each other at eight Weyl points with energies of ≈ 0.005 eV ($W1$) and ≈ 0.045 eV ($W2$), respectively. Topological Fermi arcs (highlighted by yellow curves in Fig. 2g) are expected to emerge between the Weyl points with opposite chiralities^{21,23,24}. At the energy of $W2$, part of the arcs is shadowed by the pockets and only a small portion is observed. In addition to the topological surface states, there are also trivial surface states (indicated by white arrows). Theoretical calculation also shows that in the centrosymmetric $1T'$ phase, the electron and hole pockets have no touching points, and only the trivial surface states remain (see Supplementary Fig. 1). The disappearance of the

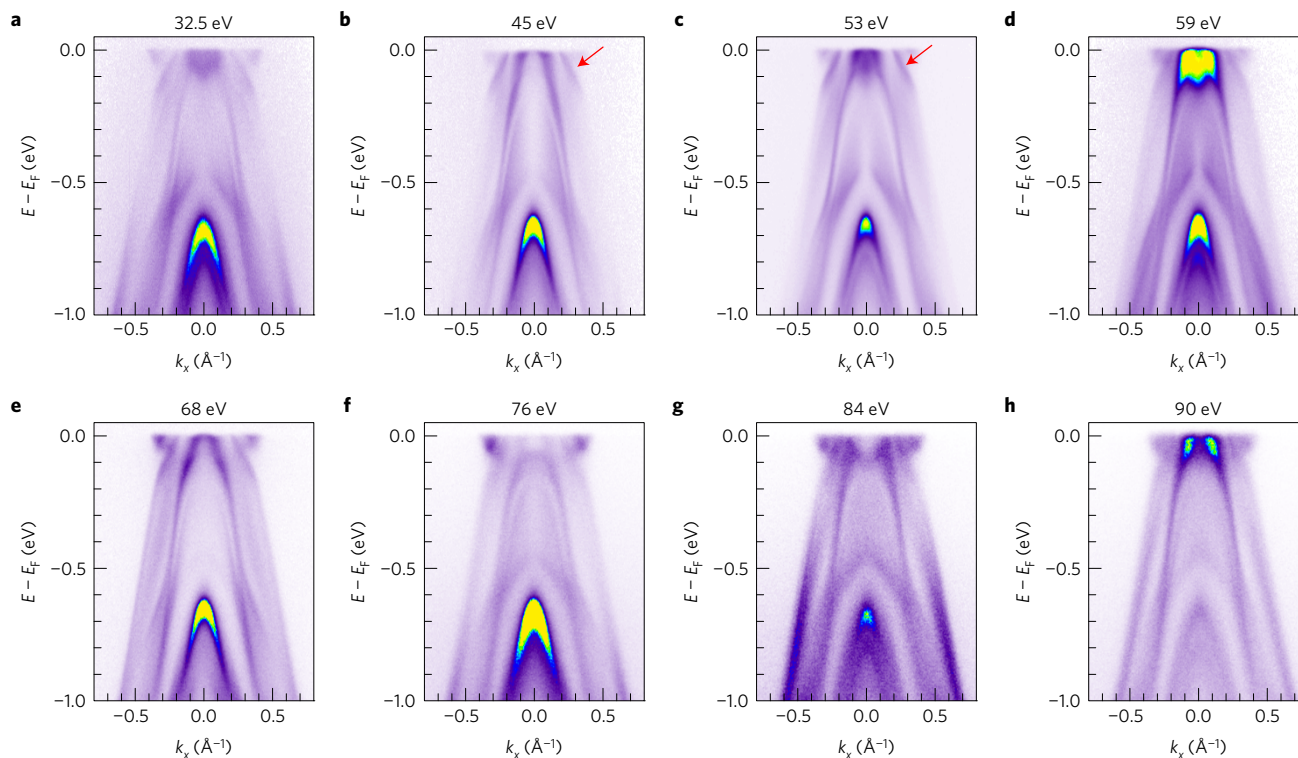


Figure 4 | Bulk states versus surface states distinguished by ARPES. a–h, Intensity maps measured along the $\bar{X}-\bar{\Gamma}-\bar{X}$ direction at selected photon energies from 32.5 eV to 90 eV. Due to the finite analyser slit width, the measured dispersion is averaged over a finite k_y momentum window (for example, $\pm 0.026 \text{ \AA}^{-1}$ at 53 eV photon energy) and the measured dispersion covers the contribution from the topological surface states that start from $k_y \approx 0.014 \text{ \AA}^{-1}$ (see Supplementary Fig. 2).

Fermi arcs in the $1T'$ phase further confirms their origin from the Weyl semi-metallic state. The characteristic electronic structure of T_d phase MoTe_2 is schematically summarized in Fig. 2h with the energies of the Weyl points as examples.

Since both the topological and the trivial surface states are squeezed in the narrow gap between the electron and hole pockets (Fig. 3a–d), resolving the different features in ARPES measurement is the most challenging aspect to correctly identify the topological Fermi arcs. We search for the topological Fermi arcs in ARPES intensity maps with a surface-sensitive UV source (penetration depth of a few ångströms). The intensity contribution from bulk bands is largely suppressed by using selected specific surface-sensitive photon energy with different polarizations, and the surface states in-between the bulk electron and hole pockets can thus become more accessible experimentally.

Figure 3e–h shows the high-resolution ARPES intensity maps taken at 32.5 eV photon energy. The arcs (indicated by red arrows) are clearly observed. At E_F (panels a,e,i) and -0.02 eV (panels b,f,j), the arcs and the trivial surface states are not well separated. However, as the electron pocket shrinks with decreasing energy, the separation between the topological Fermi arcs (red arrow in panel g and yellow arrow in panel k) and the trivial surface states (indicated by the grey arrow in panels c, g and h) becomes more pronounced. At -0.06 eV where the electron pocket completely disappears (panel d), the trivial surface states form a loop (panels d,h) and are clearly separated from the hole pocket. The evolution of the topological and trivial surface states in ARPES measurement is in good agreement with that from the band structure calculation. Furthermore, a comparison with the zoom-in calculated maps shows that the termination points of the observed arcs (panels e–h) line up with those of the calculated ones (yellow broken curves in panels i–l), explicitly supporting the presence of topological Fermi arcs.

The observed topological Fermi arcs reside on the two-dimensional crystal surface. We performed more experimental studies, including variable incident photon energy measurement and quasi-particle interference in real space, to support the surface nature of the observed electronic feature. Bulk states with different k_z values selectively respond to different incident photon energy, which helps to separate the contributions from bulk and surface states. Figure 4a–h shows ARPES data measured along the $\bar{X}-\bar{\Gamma}-\bar{X}$ direction with photon energies from 32.5 eV to 90 eV. The dispersions near the $\bar{\Gamma}$ point change significantly with incident photon energy, suggesting that they are from bulk states. In contrast, the previously identified surface band (between E_F and -0.1 eV and indicated by red arrows in panels b and c) appears at the same position with different photon energies. Consistently, this surface band is most clearly observed at 45 eV and 53 eV, where the penetration depth of photons reaches the minimum.

The complementary surface-sensitive probe STM provides further independent experimental evidence to support the surface nature of the arcs. Universal signatures of topological Fermi arcs in quasi-particle interference (QPI) on the surface of Weyl semimetals have been theoretically established by ref. 25. Various defects on the surface elastically scatter the electrons and induce the QPI pattern. In the surface Brillouin zone, the extremal pairs of \mathbf{k}_i and \mathbf{k}_f on a two-dimensional constant energy contour, where \mathbf{k}_i and \mathbf{k}_f are the initial and final wavevectors, contribute dominantly to the spatial interference pattern of the local electron density of states³⁶. The spatial variation of the local density of states at a certain energy is the sum of the contributions from all of the extremal pairs on the constant energy contour and measured by the differential conductance (dI/dV) mapping with spatial resolution. The features in the Fourier transform of dI/dV mapping correspond to the scattering vector $\mathbf{Q} = \mathbf{k}_f - \mathbf{k}_i$ of the extremal pairs. QPI is more sensitive to the surface states or states with small k_z dependence

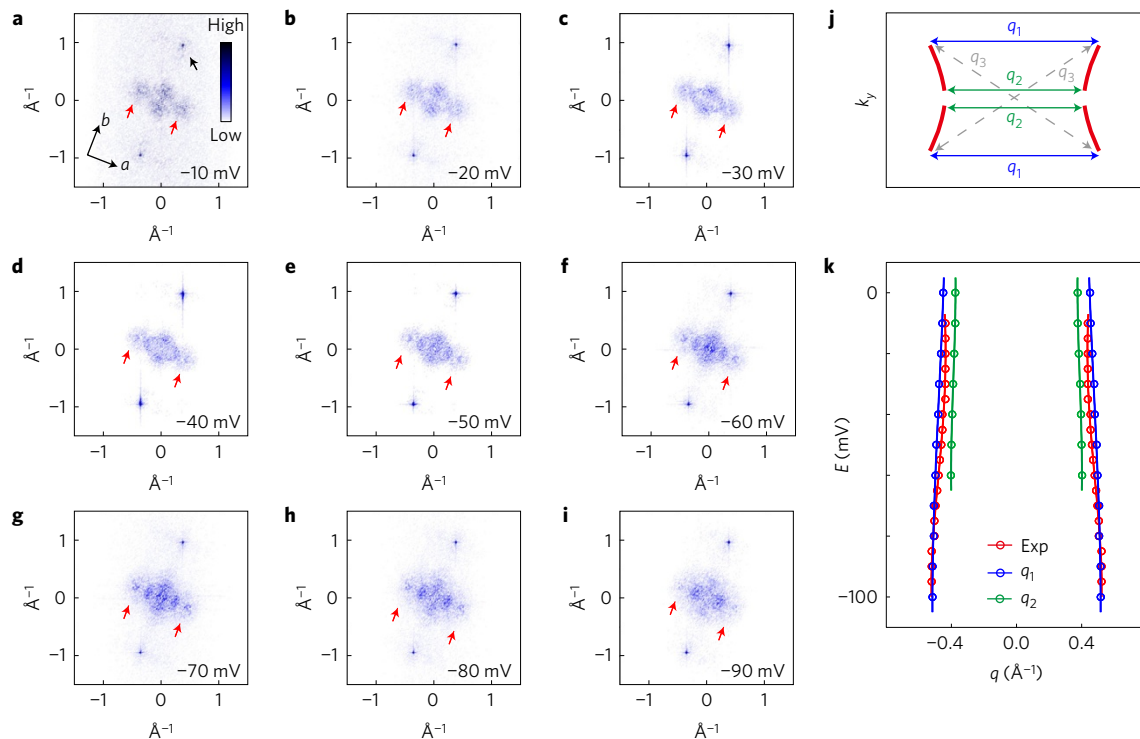


Figure 5 | Quasi-particle interference pattern. **a–i**, The FFT power spectra of the dI/dV maps of a region shown in the Supplementary Information. The current was set at 0.1 nA. Each map has 256×256 pixels. The temperature is 4.2 K. The features produced by Fermi arcs are indicated by red arrows. The origin of the additional features in the QPI needs further investigation. The black arrow points to a Bragg peak. **j**, The extremal pairs owing to a pair of topological Fermi arcs. **k**, Dispersions extracted from QPI and comparison with the calculated q_1 and q_2 . The topological Fermi arcs at positive and negative k_y values merge beyond -0.06 eV, and therefore q_2 is plotted only down to -0.06 eV.

than to the bulk ones with strong k_z dependence since the latter cannot host the ‘extreme pairs’. In this sense, QPI is advantageous in studying type-II Weyl semimetal MoTe_2 , where the topological Fermi arcs and the projected bulk pockets are very close in energy.

Figure 5a–i displays the fast Fourier transform (FFT) of the dI/dV maps between -10 mV and -90 mV. For a pair of topological Fermi arcs, three scattering wavevectors (Fig. 5j), labelled q_1 , q_2 and q_3 , might be expected to appear in QPI. Among them, q_3 is forbidden due to the requirement of the time-reversal symmetry in the system. Similar forbidden scattering was also experimentally observed in the surface states of topological insulators with time-reversal symmetry³⁷. The scattering wavevectors should generate visible features centred between q_1 and q_2 and along the Γ –X direction (Fig. 5j). Such features are clearly resolved and indicated by red arrows in FFT. The existence of such a pattern beyond the band bottom of the trivial surface states (-60 mV) excludes the possibility of trivial surface states as the origin. Moreover, the dispersions extracted from the energy-dependent scattering wavevector (panel k) are in very good agreement with the q_1 and q_2 extracted from band structure calculation, providing further independent and strong evidence for the existence of topological surface states. By combining two complementary surface-sensitive experimental probes—STM, ARPES—with theoretical calculations, we provide direct and strong experimental evidence for the existence of the topological surface states, establishing it as a type-II Weyl semimetal.

Note added in proof: During revision of this manuscript for resubmission, we became aware of related work^{38,39}.

Methods

Methods, including statements of data availability and any associated accession codes and references, are available in the online version of this paper.

Received 29 January 2016; accepted 26 July 2016;
published online 5 September 2016

References

- Nielsen, H. B. & Ninomiya, M. The Adler-Bell-Jackiw anomaly and Weyl fermions in a crystal. *Phys. Lett. B* **130**, 389–396 (1983).
- Wan, X., Turner, A. M., Vishwanath, A. & Savrasov, S. Y. Topological semimetal and Fermi-arc surface states in the electronic structure of pyrochlore iridates. *Phys. Rev. B* **83**, 205101 (2011).
- Burkov, A. A. & Balents, L. Weyl semimetal in a topological insulator multilayer. *Phys. Rev. Lett.* **107**, 127205 (2011).
- Xu, G., Weng, H., Wang, Z., Dai, X. & Fang, Z. Chern semimetal and the quantized anomalous Hall effect in HgCr_2Se_4 . *Phys. Rev. Lett.* **107**, 186806 (2011).
- Yang, K. Y., Lu, Y. M. & Ran, Y. Quantum Hall effects in a Weyl semimetal: possible application in pyrochlore iridates. *Phys. Rev. B* **84**, 075129 (2011).
- Hosur, P. & Qi, X. Recent developments in transport phenomena in Weyl semimetals. *C. R. Phys.* **14**, 857–870 (2013).
- Zhang, H., Wang, J., Xu, G., Xu, Y. & Zhang, S. C. Topological states in ferromagnetic CdO/EuO superlattices and quantum wells. *Phys. Rev. Lett.* **112**, 096804 (2014).
- Liu, J. & Vanderbilt, D. Weyl semimetals from noncentrosymmetric topological insulators. *Phys. Rev. B* **90**, 155316 (2014).
- Hirayama, M., Okugawa, R., Ishibashi, S., Murakami, S. & Miyake, T. Weyl node and spin texture in trigonal tellurium and selenium. *Phys. Rev. Lett.* **114**, 206401 (2015).
- Weng, H., Fang, C., Fang, Z., Bernevig, B. A. & Dai, X. Weyl semimetal phase in noncentrosymmetric transition-metal monophosphides. *Phys. Rev. X* **5**, 011029 (2015).
- Huang, S.-M. *et al.* A Weyl Fermion semimetal with surface Fermi arcs in the transition metal monophosphide TaAs class. *Nat. Commun.* **6**, 7373 (2015).
- Ruan, J. *et al.* Symmetry-protected ideal Weyl semimetal in HgTe-class materials. *Nat. Commun.* **7**, 11136 (2016).
- Weyl, H. Elektron und gravitation I. *Z. Phys.* **56**, 330–352 (1929).
- Xu, S.-Y. *et al.* Discovery of a Weyl fermion semimetal and topological Fermi arcs. *Science* **349**, 613–617 (2015).

15. Lv, B. Q. *et al.* Experimental discovery of Weyl semimetal TaAs. *Phys. Rev. X* **5**, 031013 (2015).
16. Yang, L. X. *et al.* Weyl semimetal phase in the non-centrosymmetric compound TaAs. *Nat. Phys.* **11**, 728–732 (2015).
17. Son, D. T. & Spivak, B. Z. Chiral anomaly and classical negative magnetoresistance of Weyl metals. *Phys. Rev. B* **88**, 104412 (2013).
18. Huang, X. *et al.* Observation of the chiral-anomaly-induced negative magnetoresistance in 3D Weyl semimetal TaAs. *Phys. Rev. X* **5**, 031023 (2015).
19. Zhang, C. *et al.* Signatures of the Adler-Bell-Jackiw chiral anomaly in a Weyl fermion semimetal. *Nat. Commun.* **7**, 10735 (2016).
20. Jian, S. K., Jiang, Y. F. & Yao, H. Emergent spacetime supersymmetry in 3D Weyl semimetals and 2D Dirac semimetals. *Phys. Rev. Lett.* **114**, 237001 (2015).
21. Soluyanov, A. A. *et al.* Type-II Weyl semimetals. *Nature* **527**, 495–498 (2015).
22. Xu, Y., Zhang, F. & Zhang, C. Structured Weyl points in spin-orbit coupled fermionic superfluids. *Phys. Rev. Lett.* **115**, 265304 (2015).
23. Sun, Y., Wu, S. C., Ali, M. N., Felser, C. & Yan, B. Prediction of Weyl semimetal in orthorhombic MoTe₂. *Phys. Rev. B* **92**, 161107 (2015).
24. Wang, Z. *et al.* MoTe₂: a type-II Weyl topological metal. *Phys. Rev. Lett.* **117**, 056805 (2016).
25. Kourtis, S., Li, J., Wang, Z., Yazdani, A. & Bernevig, B. A. Universal signatures of Fermi arcs in quasiparticle interference on the surface of Weyl semimetals. *Phys. Rev. B* **93**, 041109 (2016).
26. Ali, M. N. *et al.* Large, non-saturating magnetoresistance in WTe₂. *Nature* **514**, 205–208 (2014).
27. Chang, T.-R. *et al.* Prediction of an arc-tunable Weyl fermion metallic state in Mo_xW_{1-x}Te₂. *Nat. Commun.* **7**, 10639 (2016).
28. Qi, Y. *et al.* Superconductivity in Weyl semimetal candidate MoTe₂. *Nat. Commun.* **7**, 11038 (2016).
29. Pletikosić, I., Ali, M. N., Fedorov, A. V., Cava, R. J. & Valla, T. Electronic structure basis for the extraordinary magnetoresistance in WTe₂. *Phys. Rev. Lett.* **113**, 216601 (2014).
30. Wu, Y. *et al.* Temperature-induced Lifshitz transition in WTe₂. *Phys. Rev. Lett.* **115**, 166602 (2015).
31. Jiang, J. *et al.* Signature of strong spin-orbital coupling in the large nonsaturating magnetoresistance material WTe₂. *Phys. Rev. Lett.* **115**, 166601 (2015).
32. Beloposki, I. *et al.* Fermi arc electronic structure and Chern numbers in the type-II Weyl semimetal candidate Mo_xW_{1-x}Te₂. *Phys. Rev. B* **94**, 085127 (2016).
33. Clarke, R., Marseglia, E. & Hughes, H. P. A low-temperature structural phase transition in β-MoTe₂. *Philos. Mag. B* **38**, 121–126 (1978).
34. Manolikas, C., Van Landuyt, J. & Amelinckx, S. Electron microscopy and electron diffraction study of the domain structures, the dislocation fine structure, and the phase transformations in β-MoTe₂. *Phys. Status Solidi* **53**, 327–338 (1979).
35. Keum, D. H. *et al.* Bandgap opening in few-layered monoclinic MoTe₂. *Nat. Phys.* **11**, 482–486 (2015).
36. Wang, J. *et al.* Power-law decay of standing waves on the surface of topological insulators. *Phys. Rev. B* **84**, 235447 (2011).
37. Zhang, T. *et al.* Experimental demonstration of topological surface states protected by time-reversal symmetry. *Phys. Rev. Lett.* **103**, 266803 (2009).
38. Huang, L. *et al.* Spectroscopic evidence for a type II Weyl semimetallic state in MoTe₂. *Nat. Mater.* <http://dx.doi.org/10.1038/nmat4685> (2016).
39. Xu, S.-Y. *et al.* Discovery of Lorentz-violating Weyl fermion semimetal state in LaAlGe materials. Preprint at <http://arXiv.org/abs/1603.07318> (2016).

Acknowledgements

This work is supported by the National Natural Science Foundation of China (grant no. 11274191, 11334006), Ministry of Science and Technology of China (no. 2015CB92100, 2016YFA0301004 and 2012CB932301) and Tsinghua University Initiative Scientific Research Program (no. 2012Z02285). The Advanced Light Source is supported by the Director, Office of Science, Office of Basic Energy Sciences, of the US Department of Energy under contract no. DE-AC02-05CH11231.

Author contributions

S.Z., X.C. and Y.W. conceived the research project. K.D. and K.Z. grew and characterized the samples under the supervision of Y.W. K.D., G.W., K.Z., S.D., E.W., M.Y. and Hongyun Z. performed the ARPES measurements and analysed the ARPES data. J.D. and A.F. provided support for the ARPES experiments. P.D. and Z.X. performed the STM measurements. Haijun Z. performed the first-principles calculations presented in the manuscript. H.H. and W.D. repeated the calculation. K.D., H.Yao, Y.W., X.C. and S.Z. wrote the manuscript, and all authors commented on the manuscript.

Additional information

Supplementary information is available in the online version of the paper. Reprints and permissions information is available online at www.nature.com/reprints. Correspondence and requests for materials should be addressed to Y.W., X.C. or S.Z.

Competing financial interests

The authors declare no competing financial interests.

Methods

Sample growth. High-quality β - MoTe_2 single crystals were grown by chemical vapour transport using polycrystalline MoTe_2 as precursors. Polycrystalline MoTe_2 was synthesized by directly heating the stoichiometric mixture of high-purity Mo foil (99.95%, Alfa Aesar) and Te ingot (99.99%, Alfa Aesar) at 1,073 K in a vacuum-sealed silica ampoule for 3 days. The as-grown MoTe_2 was then recrystallized by the chemical vapour transport method using powder TeCl_4 (99%, Aladdin) as the transporting agent with a concentration of $\leq 2.7 \text{ mg ml}^{-1}$. Material transport occurred in a sealed silica ampoule in a tube furnace for 3 days. After the reaction, the ampoule was immediately quenched in cold water to obtain large-size β - MoTe_2 single crystals.

ARPES measurement. Bulk-sensitive laser-ARPES measurements have been performed in the home laboratory at Tsinghua University with a fourth harmonic generation light source. Surface-sensitive ARPES measurements have been performed at BL4.0.1 and BL12.0.1 of the Advanced Light Source using photon energies from 30.5 eV to 90 eV. The overall experimental energy resolution at 32.5 eV is better than 18 meV. The samples were cleaved and measured at 10–20 K in the T_d phase.

STM measurement. STM experiments were conducted on a Unisoku ultrahigh-vacuum low-temperature (down to 4.2 K) system equipped with an *in situ* cleaving stage. The MoTe_2 single crystals were cleaved in ultrahigh vacuum

(5×10^{-11} torr) at room temperature and then transferred to STM to perform measurement at 4.2 K with a PtIr tip. QPI maps and dI/dV spectra were acquired using a lock-in amplifier at a frequency of 913 Hz.

First-principles calculations. The *ab initio* calculations are carried out in the framework of the Perdew–Burke–Ernzerhof-type generalized gradient approximation of the density functional theory through employing the Vienna *Ab initio* simulation package (VASP)⁴⁰ with the projected augmented wave (PAW) method. The kinetic energy cutoff is fixed to 400 eV, and the k -point mesh is taken as $12 \times 10 \times 6$ for the bulk calculations. The spin–orbit coupling effect is self-consistently included. The lattice constants are taken from experiments²³, but the atoms in the unit cell are fully relaxed with the force cutoff 0.01 eV \AA^{-1} . Maximally localized Wannier functions are employed to obtain the *ab initio* tight-binding model of semi-infinite systems with the (001) surface as the boundary to exhibit surface states and topological Fermi arcs. An iterative method is used to obtain the surface Green's function of the semi-infinite system.

Data availability. The data that support the plots within this paper and other findings of this study are available from the corresponding author on request.

References

40. Kresse, G. & Furthmüller, J. Efficient iterative schemes for *ab initio* total-energy calculations using a plane-wave basis set. *Phys. Rev. B* **54**, 11169 (1996).